Structure determination of helical filaments by solid-state NMR spectroscopy

Lichun He[a,1], Benjamin Bardiaux[b,1], Mumdooh Ahmed[a,c,2], Johannes Spehr[a], Renate König[d], Heinrich Lünsdorf[e], Ulfert Rand[f], Thorsten Lührs[g], and Christiane Ritter[a,2,3]

[a]Laboratory for Macromolecular Interactions, Helmholtz Centre for Infection Research, 38124 Braunschweig, Germany; [b]Unité de Bioinformatique Structurale, CNRS UMR 3528, Institut Pasteur, 75015 Paris, France; [c]Department of Physics, Faculty of Science, Suez University, Suez, 43533, Egypt; [d]Research Group "Host-Pathogen Interactions", Paul-Ehrlich-Institut, 63225 Langen, Germany; [e]Central Unit for Microscopy, Helmholtz Centre for Infection Research, 38124 Braunschweig, Germany; [f]Immune Aging and Chronic Infection, Helmholtz Centre for Infection Research, 38124 Braunschweig, Germany; and [g]SeNostic GmbH, 38124 Braunschweig, Germany

The controlled formation of filamentous protein complexes plays a crucial role in many biological systems and represents an emerging paradigm in signal transduction. The mitochondrial antiviral signaling protein (MAVS) is a central signal transduction hub in innate immunity that is activated by a receptor-induced conversion into helical superstructures (filaments) assembled from its globular caspase activation and recruitment domain. Solid-state NMR (ssNMR) spectroscopy has become one of the most powerful techniques for atomic resolution structures of protein fibrils. However, for helical filaments, the determination of the correct symmetry parameters has remained a significant hurdle for any structural technique and could thus far not be precisely derived from ssNMR data. Here, we solved the atomic resolution structure of helical MAVS^{CARD} filaments exclusively from ssNMR data. We present a generally applicable approach that systematically explores the helical symmetry space by efficient modeling of the helical structure restrained by interprotomer ssNMR distance restraints. Together with classical automated NMR structure calculation, this allowed us to faithfully determine the symmetry that defines the entire assembly. To validate our structure, we probed the protomer arrangement by solvent paramagnetic resonance enhancement, analysis of chemical shift differences relative to the solution NMR structure of the monomer, and mutagenesis. We provide detailed information on the atomic contacts that determine filament stability and describe mechanistic details on the formation of signaling-competent MAVS filaments from inactive monomers.

solid-state NMR | protein structure | grid search | MAVS | innate immunity

Large higher-order protein assemblies play pivotal roles in diverse biological systems. Most of these assemblies, such as cytoskeleton filaments, fibrils, flagella, viral capsids, and the newly emerging cellular signaling machineries (1), are composed of repetitive and symmetrically arranged building blocks, the protomers. Typically, their sizes and often filamentous natures render them refractory to X-ray crystallography and solution NMR. Electron microscopy (EM) studies have provided valuable structural information. However, thus far, only few cryo-EM structures could be obtained with sufficient resolution to decipher fine details of the interprotomer contacts (2, 3). In addition, ambiguities in the determination of the helical symmetries have occasionally given rise to contradictory structural models (4–8). In the last decade, magic angle spinning solid-state NMR (ssNMR) has become a powerful technique to determine atomic resolution structures of protein filaments, in particular of amyloid fibrils (9–14). ssNMR has been successfully combined with cryo-EM data and computational approaches to determine the helical filament structure of the type III secretion needle (15, 16), and ssNMR distance restraints allowed to further refine the interprotomer contacts (16, 17). In general, helical filaments are particularly challenging because of restraint ambiguities inherent to homo-oligomeric assemblies, the large, and varying, number of interacting protomers and the ensuing size of the atomic complex to be modeled, and because the symmetry is defined by numerous parameters, most importantly the rotational

twist (around the helical axis) and the translational rise (along the axis) between two subunits, the radius and the number of strands defining the helical assembly (18). Without prior knowledge of these parameters from complementary structural techniques, the conformational space to be explored can easily become intractable.

In innate immunity, the detection of viral RNA by retinoic acid inducible gene I (RIG-I)–like receptors converts the inactive, monomeric form of the mitochondrial antiviral signaling protein (MAVS) into high-molecular weight filaments that activate IFN signaling pathways (19). Although the N-terminal caspase recruitment domain (CARD) of MAVS (MAVS^{CARD}) is necessary and sufficient for filament formation, downstream signaling is mediated by the more flexible C-terminal region of MAVS (19). The filaments are propagated in a prion-like manner and can be induced by the tandem CARDs of RIG-I-like receptors or by preformed MAVS^{CARD} filaments (20). CARDs belong to the death domain superfamily of protein–protein interaction domains, which share a common six-helix bundle fold and form homo- and hetero-oligomeric structures with variable symmetry (21). The crystal structure of monomeric MAVS^{CARD} fused to

Significance

The mitochondrial antiviral signaling protein (MAVS) belongs to the emerging class of higher-order signaling machines that adopt a filamentous state on activation and propagate in a prion-like manner. Structures of helical filaments are challenging due to their size and variable symmetry parameters, which are notoriously difficult to obtain, but are a prerequisite for structure determination by electron microscopy and by solid-state NMR. Here we describe a strategy for their efficient de novo determination by a grid-search approach based exclusively on solid-state NMR data. In combination with classical NMR structure calculation, we could determine the atomic resolution structure of fully functional filaments formed by the globular caspase activation and recruitment domain of MAVS. A careful validation highlights the general applicability of this approach.

maltose binding protein is available (22), and we have previously presented the sequence-specific secondary structure of this domain in its filamentous form (23). Two competing structural models of MAVS^{CARD} filaments derived from cryo-EM reconstructions were published last year (5, 6).

Here we present a generally applicable strategy to derive the symmetry parameters of helical filaments exclusively from ssNMR-derived data and use this strategy to determine the atomic resolution structure of MAVS^{CARD} filaments. We show that the helical symmetry parameters and handedness can be faithfully derived from interprotomer ssNMR distance restraints. In addition, we used solution NMR, paramagnetic relaxation enhancement (PRE), and mutagenesis to validate our approach and to unravel details of the MAVS^{CARD} assembly mechanism.

Results

Distance Restraints from ssNMR Spectroscopy. Isotope-labeled WT MAVS^{CARD} filaments were purified under nondenaturing conditions from *Escherichia coli*. These filaments induced MAVS-mediated IFN stimulation when electroporated into a reporter cell line (Fig. S1 *A–F*), indicating that they were fully functional and structurally compatible with endogenous full-length MAVS. In homo-oligomeric assemblies, distance restraints observed in uniformly isotope labeled samples may arise either from inter- or intraprotomer contacts. We thus based our structure determination strategy on a set of dilute (9) and mixed isotope-labeled samples (15, 24). To prepare these, we made use of our observation that MAVS^{CARD} filaments could be reversibly disassembled into monomers and reassembled into filaments by changing buffer pH. To confirm that the monomer remained structurally unchanged at low pH, we determined the solution NMR structure of monomeric MAVS^{CARD} at pH 3.0 and compared it with the X-ray structure determined at neutral pH 8.5 (Table S1 and Fig. S1*G*). We also found no effect on the assembly pattern of the filaments as evidenced by negative stain EM images and 2D ^{13}C-^{13}C proton-driven spin diffusion (PDSD) spectra on uniformly ^{13}C,^{15}N-labeled MAVS^{CARD} filaments before and after reassembly (Fig. S1 *H–J*). As no evidence has yet been found, by us or others, for smaller stable oligomeric species, we consider a single MAVS^{CARD} molecule as the protomeric unit within the filament.

The resonance assignment had been previously achieved on a single, uniformly ^{13}C,^{15}N-labeled sample (23). Dihedral angles and H-bonds were calculated from the chemical shifts of backbone nuclei with TALOS+ (25). MAVS^{CARD} has excellent spectroscopic properties with good line widths of ~75–80 Hz even for uniformly ^{13}C-labeled samples ([UL-^{13}C$_6$]Glc) (Fig. S2*A*), suggesting a reproducibly high degree of microscopic order within the NMR samples. This high spectroscopic quality allowed the unambiguous determination of many intraresidue and sequential cross-peaks from a set of dipolar-assisted rotational resonance (DARR) experiments with short mixing times (Table S1), as well as from 3D NCACX and NCOCX spectra (Fig. 1 *F* and *G*). Assignments were considered to be unambiguous if they were either frequency unambiguous within a ±0.21-ppm tolerance window or supported by an extensive network of intraresidue and sequential restraints (Fig. 1 *F* and *G*). Short- and medium-range restraints could be unambiguously assigned using these criteria. However, spectral crowding would severely complicate the unambiguous manual assignment of further medium- and long-range restraints, and additional ambiguities exist in homo-oligomeric assemblies as cross-peaks could arise either from intra- or interprotomer contacts. Thus, we used a strategy that relies on sparse ^{13}C-labeling to reduce spectroscopic assignment ambiguities (26, 27) and on mixed samples with differential isotopic labeling patterns to distinguish between intra-and interprotomer cross-peaks (Fig. 2 and Fig. S2). To achieve the latter, we recorded long mixing time DARR and PDSD spectra on samples that were labeled with ^{15}N and either [UL-^{13}C$_6$]Glc, [1-^{13}C]Glc, or [2-^{13}C]Glc and compared

them to a 400-ms DARR spectrum of a [UL-^{13}C$_6$]Glc-labeled sample that was diluted 1:6 with unlabeled MAVS^{CARD}. Any cross-peak that was absent in the diluted sample was considered to be potentially interprotomer and was removed from the set of restraints used for the protomer structure calculation. In addition, a PDSD spectrum was recorded on a 1:1 mixture of [1-^{13}C]Glc and [2-^{13}C]Glc-labeled MAVS^{CARD}. Any resonance present in this spectrum, but not in the spectra of the individual [1-^{13}C]Glc and [2-^{13}C]Glc samples, was also removed from the set of intraprotomer cross-peaks (Fig. 2). To achieve unambiguous assignments of medium- and long-range restraints from this set, we relied on the long mixing time PDSD and on proton-assisted insensitive nuclei (PAIN) spectra of the sparsely labeled samples. These spectra exhibited significantly improved ^{13}C line widths of 40–45 Hz and chemical shift deviations of less than 0.04 ppm for intraresidual and sequential cross-peaks (26, 27). Thus, we could assign 859 short- and medium-range intraprotomer distance restraints and 64 long-range ones (Table S2) either as frequency-unambiguous within a ±0.12-ppm tolerance window (Fig. 1 *A–C*) or, in cases where no more than three assignment options existed within this tolerance window, assignments were accepted as network unambiguous if there is extensive restraints (>3) between the two residues and if supported by other unambiguously assigned cross-peaks. The calculation of the protomer structure made use of in total 923 unambiguous restraints along with additional 2,185 ambiguous restraints.

Interprotomer distance restraints are of crucial importance for the calculation of the filament structure. Thus, cross-peaks were considered and accepted as unambiguous interprotomer restraints only if they met the following two criteria: (*i*) cross-peak is absent in the spectrum of the 1:6 diluted [UL-^{13}C$_6$]Glc sample (Fig. 3 *A* and *C*) or present only in the spectrum of the mixed [(1/2)-^{13}C]Glc labeled sample (Fig. 3*B*) and (*ii*) frequency-unambiguous assignment within a ±0.12-ppm tolerance window (Fig. 3 *A–D*) or network unambiguous as defined above; most cross-peaks were further substantiated by one of the following criteria: (*iii*) at least two unambiguous cross-peaks for each pair of residues (Fig. 3 *A–D*) and (*iv*) resonances in PAIN-CP spectra of [1-^{13}C]Glc and [2-^{13}C]Glc labeled samples (Fig. 3 *E* and *F*) were incompatible with the protomer structure, leaving only frequency-unambiguous interprotomer assignment options. In total, 51 interprotomer distance restraints were identified, of which 36 were unambiguous, relating to 15 pairs of interacting residues (Table S2). Fifteen more had two to eight interprotomer assignment options (Fig. S3 *A* and *H*).

Three-Step Structure Calculation of MAVS^{CARD} Filaments. To determine the 3D atomic resolution structure of MAVS^{CARD} helical filaments without prior structural knowledge, we conceived a three-step approach of (*i*) protomer structure determination, (*ii*) determination of helical symmetry parameters from interprotomer distance restraints via grid-search, and (*iii*) semiflexible calculation of the complete filament structure. This approach efficiently exploits the symmetric properties of the filamentous complex to unambiguously determine its unknown helical parameters (Fig. 4*A*). First, we used established iterative ARIA (28) protocols to determine the structure of the protomer from dihedral angles, H-bonds, and intraprotomer distance restraints. The ensemble of protomers is very well converged with a backbone RMSD of 0.60 ± 0.10 Å (Table S3) and exhibits the six-helix bundle Greek-Key topology characteristic for the death domain superfamily (Fig. 1 *D* and *E* and Fig. S3 *C* and *D*). The structure of the MAVS^{CARD} protomer is based on a unique set of NMR signals with no indications for peak doubling (Fig. 1 and Fig. S2), indicating that all protomers in the filament are in the same conformation and are arranged homogeneously in a symmetrical manner along the filament axis. This finding is consistent with known structures of oligomeric complexes in the death domain superfamily, all of
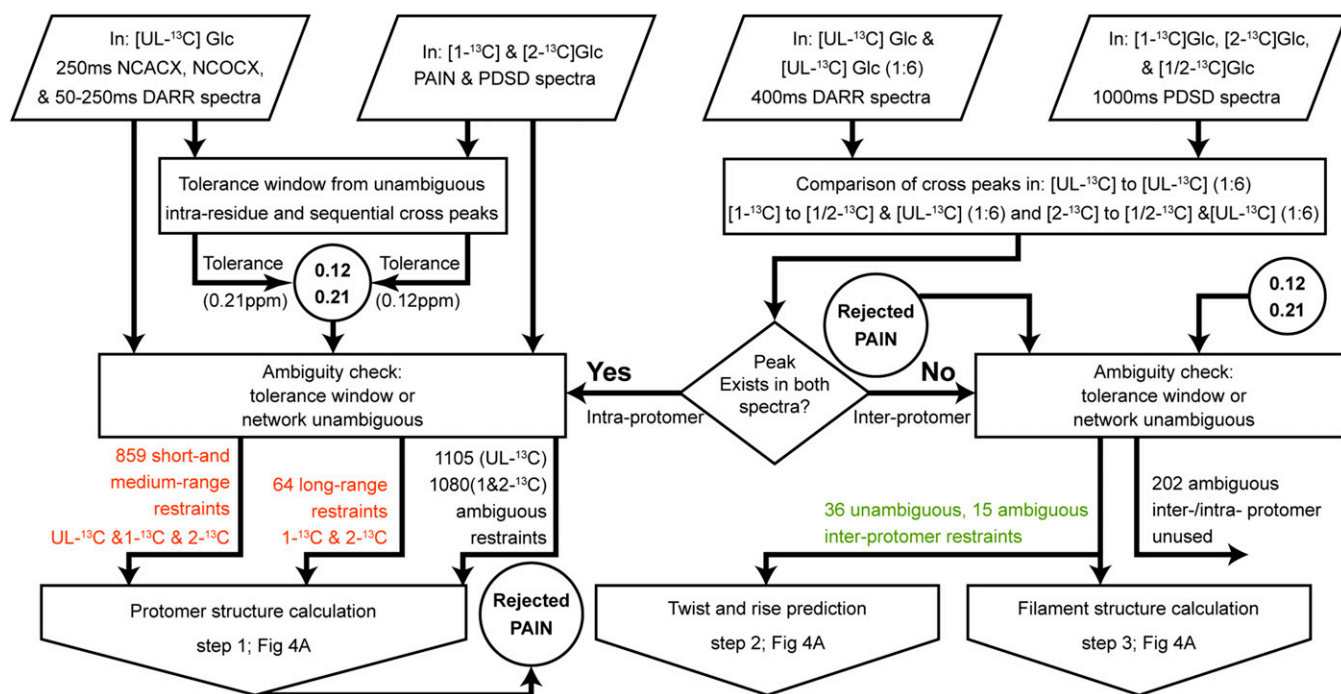
which exhibit helical or pseudohelical symmetries, albeit with variable parameters and handedness (21).

To determine the parameters defining the symmetry of the MAVS[CARD] filament, we next deviced a grid-search approach that is independent of complementary techniques for the determination of helical symmetry parameters and handedness. Instead, it makes use of interprotomer ssNMR distance restraints and systematically explores the helical space in a given range of twist and rise values (Fig. 4C). Existing grid-based methods are limited to symmetric oligomers with point symmetries (29–31). To accommodate helical symmetries, we therefore based our grid-search on a previously proposed approach for efficient modeling of symmetric oligomers from NMR data for any given fixed symmetry (32). This approach is particularly suitable for oligomers with point symmetry because the symmetry parameters can be inferred from the finite number of protomers in the oligomer. However, this is not possible for filaments with helical symmetry. Twist and rise values were thus separately and regularly incremented to generate an ensemble of helical conformations for every combination of these two parameters. Each symmetry-constrained helical conformation was determined by semiflexible energy minimization of 100 starting conformations using the previously solved protomer structure and 51 interprotomer restraints. At this stage, each interprotomer restraint was not assigned to specific protomer pairs but rather applied between a given protomer and all other protomers in the modeled filaments, in a protomer-ambiguous fashion (Fig. 5D and Table S4). In addition to left-handed and right-handed

Fig. 1. Intraprotomer distance restraints obtained in the ssNMR spectra of MAVS[CARD] filament. (A) Sections of 2D PDSD spectra of [1-13C]Glc (blue) labeled MAVS[CARD] filament. (B) Sections of 2D PDSD spectra of [2-13C]Glc (magenta) labeled MAVS[CARD] filament. (C) Sections of the 2D PAIN spectrum of [1-13C]Glc labeled MAVS[CARD] filament. The chemical shifts of 74A Cb and 89A Cb (18.54 and 18.66 ppm) and of 36A Cb and 85A Cb (19.21 and 19.33 ppm) are well distinguishable. (D and E) Structural models showing long-range intraprotomer distance restraints denoted in A and C by black boxes. (F and G) Strip plots of 3D 250-ms NCACX spectrum (teal) of [UL-13C6]-Glc labeled MAVS[CARD] filament. Unambiguous assignments of short and medium range distance restraints are indicated. Dashed lines between sequential residues highlight the dense network unambiguous assignments. All intraprotomer distance restraints are labeled as follows: short, medium (black), and long range distance restraints (red). All spectra were plotted at the same contour level; the first contour level was cut at 4.7 times the white noise level of the spectrum, and each following contour level was multiplied by 1.2. Molecular figures were prepared with the PyMOL Molecular Graphics System (Schrödinger, LLC).

Fig. 2. Flowchart of the distance restraints assignment procedure. The flowchart presents the workflow for the unambiguous and ambiguous assignment of intra- and interprotomer solid state NMR distance restraints. Input data are represented by tilted rectangles, processing steps by rectangles, conditions for decision-taking by a rhombus, intermediate outputs applied to downstream processing steps by circles, and the final output feeding into the structure determination process depicted in Fig. 4A by arrows. Numbers for unambiguous intraprotomer restraints are written in red and numbers for interprotomer restraints in green.

1-start helices, which represent the simplest description of a helical arrangement, we also tested 3-start helices with C_3 symmetry (three strands related by a threefold rotational symmetry), as previously reported by cryo-EM reconstruction (5) (Fig. 4B). Such a large grid-search can be performed because we built on an efficient approach to constrain the symmetry during the minimization (32). Here, only one protomer is explicitly (all atoms) modeled and symmetry related protomers only exist as virtual images. Because the number of strands is not a free parameter, it is required to perform separate grid-search calculations for every Cn symmetry to be probed. This approach of strict symmetry was shown to work successfully on oligomers with helical and point symmetry, and computational time is largely independent of the number of protomers (32) or strands.

The result of an initial coarse-grained grid-search with relatively large twist and rise increments yielded a very well-defined minimum of energy corresponding to a left-handed helical structure with a twist of 100° and a rise of 5.2 Å (Fig. 4D). The symmetry was further refined to a twist of 101° and rise of 5.1 Å with a finer-grained search using smaller increments on a reduced range (Fig. 4E). We confirmed the accuracy of the approach with a higher-resolution grid that converged to the very same twist and rise values (super fine-grained grid-search; Fig. 4F and Table S4). Our values are very close to the ones obtained by Wu et al. (6) (101.1° and 5.13 Å).

To further prove the applicability of our approach, we used the solution NMR structure of the MAVS^{CARD} monomer determined at low pH as input structure (Fig. S4 A and B). The symmetry parameters, and in particular the handedness, could be well approximated, indicating that our approach is not sensitive to small differences in the input monomer structure. In addition, we performed a grid-search on the type III secretion system needle (Fig. S4 C and D). The result was very close to the values obtained by Loquet et al. (15, 17), suggesting that our approach

is robust and will be generally applicable to determine the helical symmetry and the handedness of large protein assemblies.

We then determined a high-resolution structure of MAVS^{CARD} filaments using the iterative ARIA/CNS methodology (33, 34) with an extension to include helical symmetry constraints (32). This strategy allowed us to automatically assign the initially protomer-ambiguous 51 interprotomer restraints to protomers M, M ± 1, M ± 3, and M ± 4 (Fig. 6 E and F) and to reestimate the set of intraprotomer restraints in the context of the helical filament. Although no significant changes to the protomer structure were observed, the set of long-range intraprotomer restraints was increased by ~10%. Forty-three unique interprotomer restraints could be assigned unambiguously, and four more had two assignment options (Fig. S3A and Table S3). The structure of MAVS^{CARD} filaments is shown in Fig. 5 A–C. Structural statistics are given in Table S3 and Fig. S3B. The ensemble of MAVS^{CARD} structures is very well converged (backbone RMSD of 0.5 ± 0.1 Å over 21 protomers) and is very similar to the model of Wu et al. (6) when superimposing eight consecutive protomers (Fig. S3E). In this model (3J6J), only 17% of the atom pairs defined as ssNMR restraints have a distance greater than 10 Å, whereas in the 3J6C model (right-handed helix with C_3 symmetry), more than 95% do (Fig. S3G). The threshold of 10 Å (8 Å upper bound + 2 Å) was chosen to account for alternative side chain conformations in the cryo-EM structures with regards to the ssNMR structure.

The smallest entity describing all interprotomer contacts in the filament consists of four protomers M, M + 1, M + 3, and M + 4 (or, equivalently, M, M − 1, M − 3, and M − 4). Such a tetrameric subcomplex of the MAVS^{CARD} filament structure was further refined without constraining the helical symmetry. The final ensemble has a backbone RMSD of 0.7 ± 0.1 Å (Fig. 5 F and G). The average twist and rise values confirmed the fixed parameters used for the previous ARIA calculation (101 ± 1° and 5.1 ± 0.5 Å). In addition, such an ensemble provides a first approximation of the uncertainty
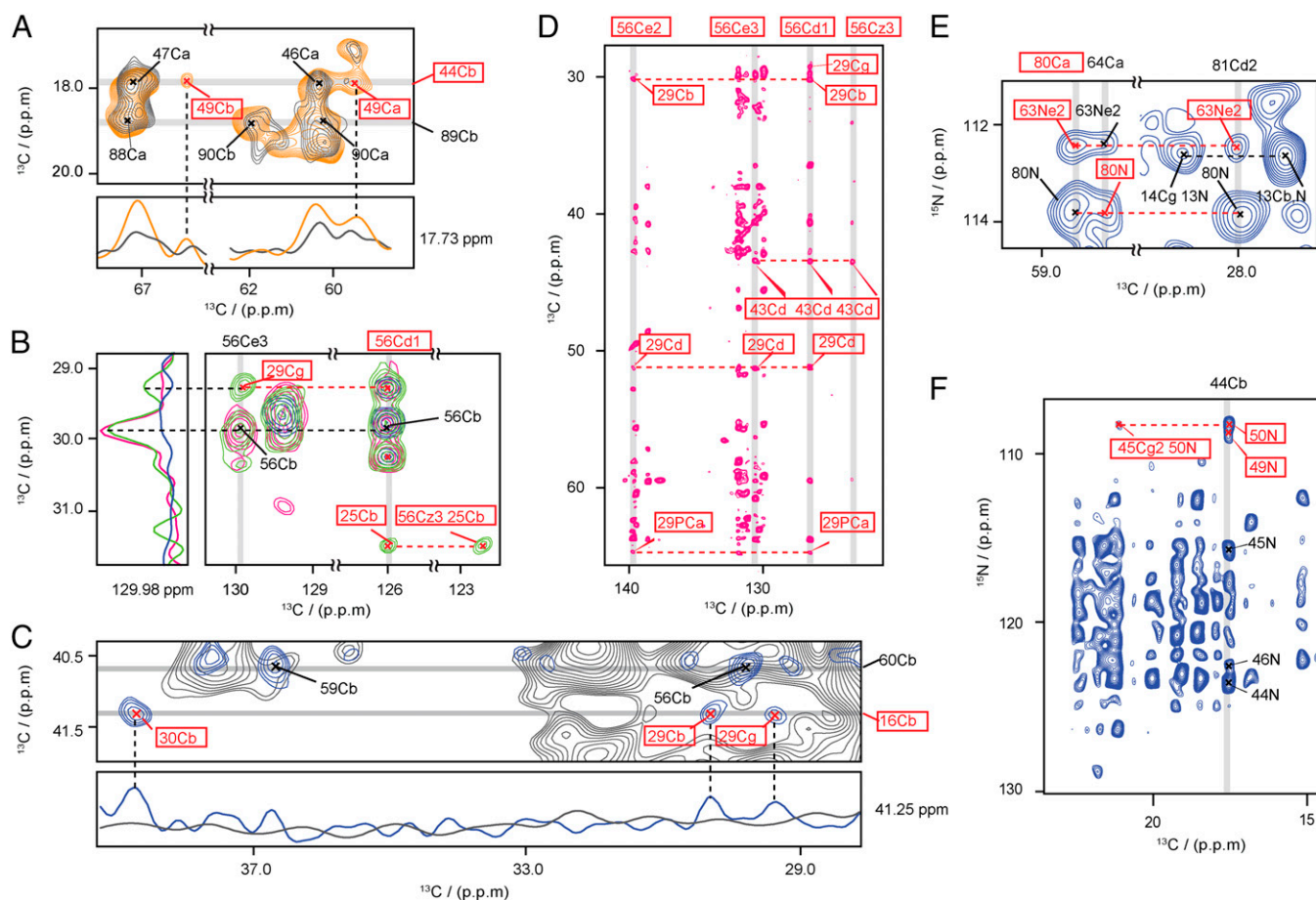
Fig. 3. Collection of interprotomer ssNMR distance restraints. All spectra were plotted at the same contour level; the first contour level was cut at 4.7 times the white noise level of the spectrum, and each following contour level was multiplied by 1.2. (*A* and *C*) Superposition of 2D ^{13}C-^{13}C correlation spectra of [1-^{13}C]Glc (blue) and [UL-^{13}C$_6$]Glc (orange) labeled MAVS^{CARD} with that of 1:6 diluted [UL-^{13}C$_6$]Glc (gray) labeled MAVS^{CARD}. 1D slices at δ_2 = 17.73 ppm (*A*) and δ_2 = 41.25 ppm (*C*) are shown with dashed line to indicate the interprotomer peaks. (*B*) Superposition of the 2D PDSD of mixed [1/2-^{13}C]Glc (green) labeled MAVS^{CARD} with the 2D PDSD of [1-^{13}C]Glc (blue) and [2-^{13}C]Glc (magenta) labeled MAVS^{CARD}. 1D traces at δ_1 = 129.9 ppm are shown with dashed line to indicate the interprotomer peaks. (*D*) Section of the 2D PDSD of [2-^{13}C]Glc (magenta) labeled MAVS^{CARD}. The network between unambiguously assigned interprotomer restraints is indicated by dashed lines. (*E* and *F*) Sections of the 2D PAIN spectrum of [1-^{13}C]Glc labeled MAVS^{CARD} containing both intra- and interprotomer distance restraints. The unambiguous restraints shown in *A* also appear in *F*. All interprotomer distance restraints are labeled in boxed red.

of the helical symmetry parameters compatible with the interprotomer distance restraints. This uncertainty was further analyzed from the super fine-grained grid-search where the spread of the twist and rise were estimated at 1.1° and 0.4 Å, respectively (Fig. S5 and *SI Text*). Although it is not possible to relate directly this data-derived uncertainty to an intrinsic feature of MAVS^{CARD} filaments, we would like to stress that a variable twist angle has been observed for some helical filaments (2, 35).

Structure of the MAVS^{CARD} Filament. The MAVS^{CARD} filament [Protein Data Bank (PDB) ID code 2MS7] has an outer diameter of ~82 Å and no inner pore. Each protomer is in contact with six other protomers via three interfaces denoted Ia/Ib, IIa/IIb, and IIIa,IIIb (Fig. 6 *A–D*), which are preserved in death domain complexes determined to date (2, 21, 36). The IIIa/IIIb interface mediates the intrastrand contacts that form the left-handed 1-start helix. It is formed by residues of the C-terminal kink of helix α1 and the loop between helices α3 and α4 (IIIa) interacting with helix α3 (Fig. 6*C*). Interstrand contacts are mediated by the Ia/Ib and IIa/IIb interfaces. Alternatively, these interfaces can be described to form a 3-start, right-handed and a 4-start, left-handed helix, respectively (Fig. 6*E*). The Ia/Ib interface is formed by residues of helices α1 and α4 interacting

with the tips of helices α2, α3 and the loop in between (Fig. 6*B*). In the IIa/IIb interface, the loop between helices α4 and α5 is in contact with the two loops connecting helices α1, α2 and α5, α6, respectively (Fig. 6*A*). Although the type II and III interfaces are dominated by polar and charged interactions, the type I interface is characterized by a mix of polar and hydrophobic interactions. In particular, the aromatic residues Y11, Y30, F16, and W56 contribute to this interface and give rise to multiple interprotomer distance restraints. The strong contribution of charged residues to all three interfaces is in agreement with our observation that MAVS^{CARD} fibrils can be disassembled at low pH and is also reflected by loss-of-activity mutants generated by us (Fig. S6 *D–G*) and others (5, 37), which often target charged residues.

Cross-Validation of the Filament Structure. Toward an unbiased validation of our final structure, we probed the orientation and packing of the protomers within the filament by two independent experiments. First, we analyzed the solvent accessibility of individual residues by measuring the PRE effect of 100 mM gadolinium diethylenetriaminepentacetate (Gd-DTPA) added to the solvent. To have at least one signal for every amino acid that could be faithfully integrated, ^{13}C-^{13}C DARR spectra and ^{15}N-^{13}C NCA spectra of MAVS^{CARD} filament were recorded in the
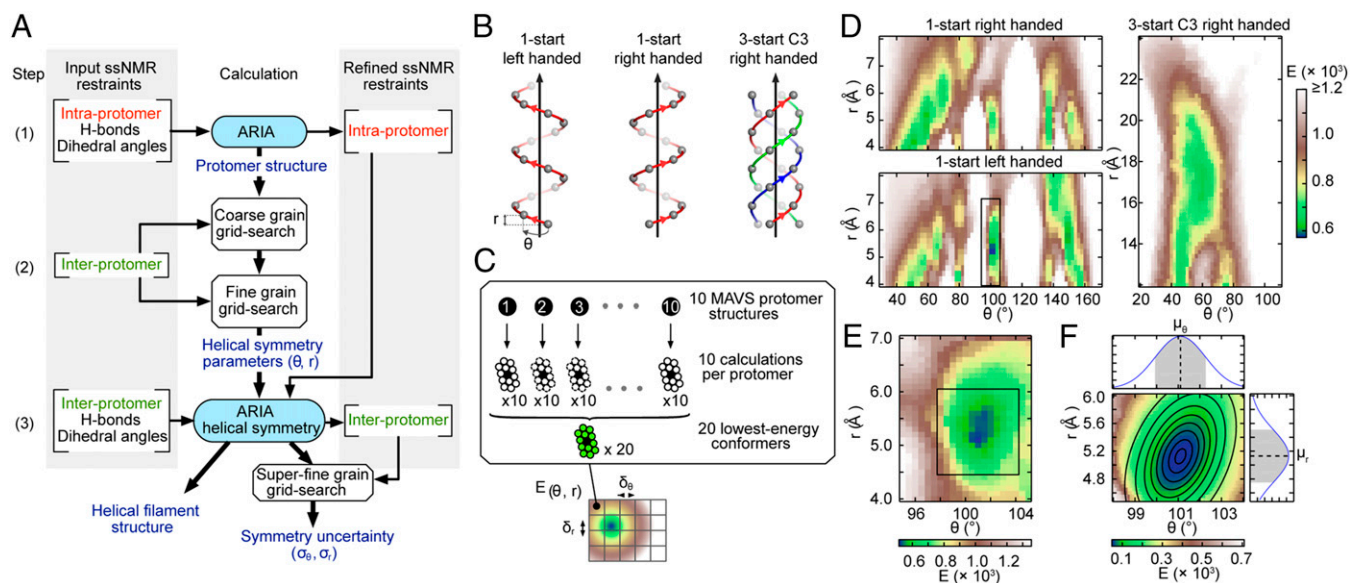
Fig. 4. Grid-search (GS) for helical symmetry and MAVS^{CARD} filament structure calculation. (*A*) Flowchart of the three-step structure calculation protocol of MAVS^{CARD} filament structure from ssNMR restraints. (*B*) Three types of helical symmetry probed in the GS approach. θ and r represent the helical twist and rise, respectively. (*C*) Schematic representation of the GS approach. The grid is filled with the median energy ($E_{(\theta,r)}$) of the 20 best helical conformers for each (θ,r) combination using $\delta\theta$ and δr increments. (*D*) Result of the coarse-grained GS. Black box indicates the region explored in the fine-grained GS. (*E*) Results of the fine-grained GS. Black box indicates the region explored in the superfine-grained GS. (*F*) Result of the superfine-grained GS with the fitted bivariate Gaussian function on $p(\theta,r)$ and the corresponding univariate Gaussian distributions for θ and r on the top and left sides, respectively.

absence and presence of Gd-DTPA (Fig. S6 *A and B*). The addition of Gd-DTPA caused considerable peak broadening, but had only marginal effects on peak positions. Fig. 7*B* shows the relative attenuation of the peak intensity along the sequence. Strikingly, these values correlate precisely with the calculated depth of the Ca atoms within the context of the filament (Fig. 7*C*), supporting the accuracy of the structure. In contrast, the same calculations for monomeric MAVS^{CARD} and for the structure of Xu et al. (PDB ID code 3J6C) (5) differ drastically from our experimental PRE data (Fig. S6*C*). To identify residues that become buried in the filament core compared with the monomeric structure, we analyzed the Ca and Cb chemical shift changes between the monomeric MAVS^{CARD} mutant D23S E26S in solution and the MAVS^{CARD} filament measured at the same buffer conditions. (Fig. 7 *A and D*). A representation of the residues affected by either PRE or by chemical shift perturbation on the protomer structure of MAVS^{CARD} shows that the data are perfectly complementary (Fig. 7 *D and E*). These experiments can thus be taken as convincing independent confirmation of the calculated structure and the validity of our approach.

Assembly Mechanism of MAVS^{CARD} Filaments. The protomer structure of MAVS^{CARD} filaments is virtually identical to the solution NMR and crystal structures of the monomeric form, with backbone RMSD values of 2.37 and 1.82 Å, respectively (Figs. S1*G* and S3 *D and F*). This observation suggests that MAVS^{CARD} monomers assemble into filaments by a rigid-body docking mechanism. The largest deviations occur in helix α3, which is deeply buried in the filament structure and contributes to both type I and type III interfaces. Residues at the N-terminus of α3 contribute most to the uncertainty of the helical symmetry determination (Fig. S5) and exhibit lower-than-average signal to noise values in the CONCA spectrum (Fig. S5*B*), indicating increased local dynamics and/or chemical exchange due to its contribution to the protomer interfaces. Among known death domain assemblies, the pyrin domains of ASC (apoptosis-associated speck-like protein containing a CARD) and AIM2 (absent in melanoma 2) form helical structures with a similar orientational

change of the helix2-helix3 loop and helix α3, suggesting that such a conformational change might facilitate the formation of the helical assembly and contribute to their plasticity (2, 38). Notably, one face of the cross section of a MAVS^{CARD} filament is highly positively charged and the opposite one is mostly negatively charged (Fig. 5*E*), which supports our notion that the charge complementarity plays an important role in the filament assembly.

To gain additional insights into the assembly mechanism, we tested a number of single and double point mutants targeting each of the six interaction sites for their ability to form filaments at neutral pH. Gel filtration using Superdex 200 showed that filament formation was impaired for all these mutants. The double mutants D23S E25S, R64S R65S, and R37S R41S were completely monomeric (Fig. S6 *D and E*). Nevertheless, all mutants impaired the ability to activate the IFN-β signaling pathway (Fig. S6 *F and G*), suggesting these interfacial residues are crucial for MAVS functionality in vivo and further confirming the validity of our structure.

Discussion

We presented an efficient approach to determine the atomic resolution structure of a helical filament based exclusively on experimental ssNMR data without using any template or input from EM other than the information that the complex has a filamentous structure. We show that helical symmetry parameters can be faithfully determined from a set of interprotomer distance restraints with moderate levels of spectroscopic ambiguity. As these are essential for our approach, sparse isotope labeling was particularly useful as it yielded high-resolution spectra, which allowed a precise assignment within a narrow ±0.12-ppm tolerance window (Fig. 1*C* and Fig. S2). The presented approach is robust in the sense that it allows the unambiguous extraction of the helical handedness. The need to determine reliable helical symmetry parameters was highlighted by the recent dispute on the correct symmetry of MAVS^{CARD} filaments analyzed by two different groups using cryo-EM (5–7).

Traditional approaches used for structure determination of proteins from NMR restraints often require the modeling of the entire
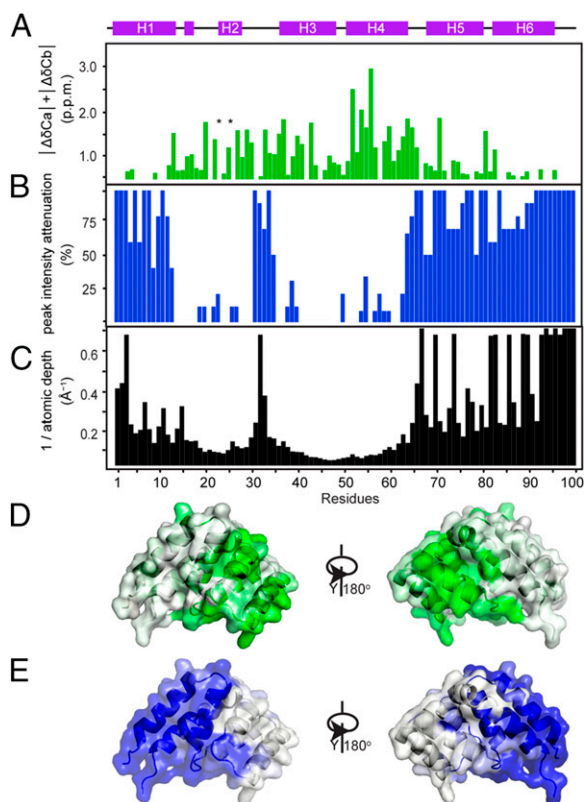
Fig. 5. Structure of MAVS^{CARD} filament calculated with ssNMR distance restraints. (*A* and *B*) Side and top views of the MAVS^{CARD} filament structure ensemble determined with ARIA. Protomers are colored as in *C*. (*C*) 2D lattice representation of the MAVS^{CARD} filament topology. Protomers are represented as hexagons, numbered according to the 1-start helix. (*D*) Restraint map of the initial (*Upper*) and final (*Lower*) set of ssNMR distance restraints. In the initial set, interprotomer restraints are ambiguous and not assigned to specific protomers. In the final set, restraints were specifically assigned by ARIA between protomers M and M + 1 (green circles), M + 3 (cyan diamonds), or M + 4 (yellow triangles). The positions of helices 1–6 of MAVS^{CARD} are shown on the top and left sides with purple boxes. (*E*) Electrostatic potential plot of MAVS^{CARD} filament. The cross sections of the electrostatic potential plot of MAVS^{CARD} filament show mostly negative charges (red) on one side and positive charges (blue) on the other side. (*F*) Cartoon representation of the ensemble of 10 refined conformers of a MAVS^{CARD} tetrameric subcomplex. The four MAVS^{CARD} protomers (M, M − 1, M − 3, and M − 4) are colored separately. For sake of clarity, C- and N-terminal residues have been removed. The average backbone RMSD of the subcomplex ensemble is 0.68 ± 0.12 Å and 0.51 ± 0.10 Å for the protomer M (residues 3–95). (*G*) Cartoon representation of the average MAVS^{CARD} tetramer structure colored by the RMS fluctuation (RMSF) among the ensemble. The largest RMSF values (red) were observed for the N-terminal parts of helix 1 and 3. Molecular figures were prepared with the PyMOL Molecular Graphics System (Schrödinger, LLC).

molecular system with all degrees of freedom. Symmetric complex structure minimization by docking is a practical alternative but usually requires the number of subunits to be known, and an unambiguous assignment of the interprotomer restraints to specific pairs of protomers. This approach was mainly demonstrated for homo-oligomers with point symmetry where only rotations are involved (39–41). Thus far, only few high-resolution structures of helical assemblies from NMR data have been published (9–14). These structures were mostly cross–β-sheet amyloid fibrils, which constitute a particular case because protomers are stacked on each

other with a helical rise corresponding to the hydrogen-bond length between β-strands of neighboring subunits (12, 42, 43). The only filamentous structures with more complex symmetries solved by ssNMR thus far are the type III secretion system needle and the M13 bacteriophage capsid that were determined using Rosetta-based approaches in combination with EM or fiber diffraction data (15, 16, 44). The Rosetta approach for oligomers combines efficient sampling of the conformational space with a physical all-atom force field that can possibly dominate over experimental input restraints (39, 45). In our approach to determine the helical symmetries, we intentionally used a simplistic force field commonly used for NMR structure determination (46). This choice ensures that the calculated oligomeric structures are predominantly the result of the experimental data, as this force field cannot effectively assess the correctness of structures by itself, and structure calculation thus relies on the input ssNMR restraints as the only attractive forces. However, this required the implementation of an efficient strategy to objectively evaluate and refine the set of NMR-derived restraints. We thus adapted the well-established ARIA approach to iteratively reassign intra- and interprotomer restraints within the context of the predetermined helical symmetry.

Additionally, our three-step strategy aims at disentangling the double problem of simultaneously finding the correct fold of the protomer and the correct arrangement of protomers. The strategy we implemented is completely automatable, which is advantageous to reduce user intervention and to ensure the objectivity and reproducibly of the calculation.

Despite their obvious significance, molecular structures of high-molecular-weight machineries are still scarce. We demonstrated

Fig. 6. Interaction interfaces involved in assembly of MAVS^{CARD} filament. (*A*–*C*) Three types of interaction interfaces were identified in the assembly of MAVS^{CARD} filament. Key residues and interprotomer ssNMR distance restraints for each interface are labeled. (*D*) Cartoon diagram of the structure of MAVS^{CARD} filament. (*E*) 2D lattice representing all three types of interfaces in the context of the MAVS^{CARD} filament. (*F*) Schematic representation of interprotomer distance restraints for the three types of interfaces. Unambiguous and ambiguous distance restraints are plotted as solid and dashed lines, respectively. The thickness of the lines is proportional to the number of restraints.

Fig. 7. Orientation of the MAVS^CARD protomer within the filament. (*A*) Sum of the absolute values of Ca and Cb chemical shift changes between monomeric MAVS^CARD mutant D25S E28S and MAVS^CARD filament. The sites of point mutants are marked (*). (*B*) Gd-DTPA–induced PRE peak intensity reduction plotted against the sequence. (*C*) The depth (Δ) of each Ca atom from the Gd-DTPA accessible surface of a MAVS^CARD protomer in the filament. For purpose of comparison with the PRE peak intensities, the inverse of the depth (1/Δ) is shown. (*D*) Residues with chemical shift differences larger than 0.4 ppm are displayed on the surface of the MAVS^CARD protomer structure in green. (*E*) Residues with a severe decrease of the peak volume (more than 50%) in the presence of Gd-DTPA are displayed on the surface of the MAVS^CARD protomer structure in blue.

an efficient ssNMR-based approach to derive not only atomic resolution structural restraints required for highest resolution structures but also the correct symmetry parameters with high fidelity. ssNMR allows for a straightforward structure validation by independent experiments such as solvent paramagnetic resonance enhancement. Our approach does not require any prior structural knowledge of the system and can be easily extended to other types of symmetry. In addition, structural information from other techniques could be efficiently implemented, thus enabling a combination of benefits from different experimental and computational techniques toward integrative approaches.

Materials and Methods

Sample Preparation. Protein expression and purification was performed as described previously (23). For solution NMR measurements, samples containing 300 μM protein were kept in 50 mM NaH$_2$PO$_4$, 1 mM DTT, pH 3, buffer with 0.01% NaN$_3$. Sparse labeling with [1 or 2-^{13}C] Glc was achieved by using [1-^{13}C] Glc or [2-^{13}C] Glc with ^{15}N-labeled ammonium chloride as the sole ^{13}C or ^{15}N source in the growth medium. A diluted sample was prepared at pH 3 by mixing of unlabeled monomeric MAVS^CARD with monomeric uniformly ^{15}N-^{13}C labeled MAVS^CARD at a molar ratio of 6:1. Then the pH of the buffer was brought back to 7 to reassemble MAVS^CARD into filaments. The [1/2-^{13}C] Glc mixed sample was prepared in the same way by mixing [1-^{13}C] Glc labeled protein with [2-^{13}C] Glc labeled protein at an equimolar ratio. Approximately 15 mg MAVS^CARD filament were packed into a 3.2-mm

thin-wall NMR rotor by centrifugation at 100,000 × g for 15 h using a specially designed filling device (47). To probe the solvent-accessible surface of the MAVS^CARD filament, 10 mL MAVS^CARD filaments (1.5 mg/mL) was incubated overnight with 100 mM Gd-DTPA and then ultracentrifuged into an ssNMR rotor at 100,000 × g for 15 h.

ssNMR Spectroscopy and Data Processing. All NMR experiments were performed on a Bruker Avance III 600-MHz spectrometer operating at a static field of 14.1 T equipped with a standard 3.2-mm Bruker triple-resonance MAS probe. All spectra were recorded at a sample temperature of 5 ± 1 °C. ^{15}N and ^{13}C transfer was established through band-selective cross-polarization, and SPINAL64 decoupling of 90 kHz was used during direct and indirect chemical shift evolution. Details of experimental parameters are described in Table S2. Chemical shift assignment was achieved in a previously described protocol with Biological Magnetic Resonance Bank (BMRB) code 25076 (23). To collect distance restraints, homonuclear 2D ^{13}C-^{13}C correlation spectra with DARR and PDSD were recorded on uniformly ^{15}N-^{13}C labeled, diluted and [1-^{13}C] Glc, [2-^{13}C] Glc sparsely labeled samples with a series of mixing times from 15 to 1,000 ms. PAIN-CP spectra were recorded on [1-^{13}C] Glc-^{15}N and [2-^{13}C] Glc-^{15}N labeled samples as previously described (48). To probe the solvent-accessible surface of the MAVS^CARD filament, ^{13}C-^{13}C DARR spectra and ^{15}N-^{13}C NCA spectra of MAVS^CARD filament were recorded in the absence and presence of 100 mM Gd-DTPA. All spectra were processed using Topspin 3.2 (Bruker Biospin) by applying squared sine bell shifted by 60° before zero filling and Fourier transformation. Polynomial baseline correction was used for both dimensions. The white noise level was calculated for all spectra as the mean root square of intensity over a wide spectral region depleted of any signal due to protein or possible spinning side band. We used an in-house written LUA script within the CARA environment to perform these calculations and mapped the obtained levels to CcpNmr for subsequent steps. Integration of peak intensities for PRE and other spectral analyses, peak picking, and assignments were performed using the CcpNmr software package (49). Peak integration was carried out in CcpNmr using the box sum volume method.

Assignment of Distance Restraints and Handling of Chemical Shift Ambiguities. Peaks were picked automatically using a threshold of 4.7 times white noise level for all spectra. Peaks corresponding to artifacts such as spinning side bands were discarded. The isotopic labeling pattern present in the [1-^{13}C]Glc and [2-^{13}C]Glc-labeled samples was determined experimentally on the basis of ^{13}C heteronuclear single quantum coherence (HSQC) spectra recorded on monomeric MAVS^CARD at pH 3, because we observed significant scrambling compared with the published basic labeling pattern. Intraresidual and sequential, as well as some medium-range, cross-peaks (between residues j and k, 2<|j–k|<4) were assigned from a series of short mixing time DARR spectra (50–250 ms) and from long mixing (250 ms) 3D NCACX and NCOCX spectra. Cross-peaks were considered as unambiguous if no other assignment options existed within a ±0.21-ppm tolerance window or if supported by an extensive network of other cross-peaks. The tolerance windows for the frequency-unambiguous assignment of cross-peaks were determined separately for uniformly and sparsely labeled samples. In both cases, we first determined the average resonance frequency and the respective chemical shift deviation for each nucleus from the intraresidual and sequential cross-peaks, averaged over all available spectra. The chemical shift deviations were less than 0.04 ppm for sparsely labeled samples and ∼0.07 ppm for uniformly labeled samples. For the manual assignment of frequency-unambiguous distance restraints, we thus chose tolerance windows of ±0.12 and ±0.21 ppm, respectively. Frequency-unambiguous long-range distance restraints were only assigned when supported in the spectra of sparsely labeled samples due to their improved resolution (Figs. 1 and 2 and Fig. S2). Additional short- and medium-range and all long-range intraprotomer distance restraints were assigned in the PDSD and PAIN spectra of [1-^{13}C]Glc and [2-^{13}C]Glc labeled sample based on the following criteria: (*i*) the cross-peaks must also be present in the 400-ms DARR spectrum of the [UL-^{13}C$_6$]Glc 1:6 diluted sample; (*ii*) the cross-peak is defined as frequency-unambiguous if no other assignment options exist within the tolerance window; and (*iii*) the cross-peak is classified as network-unambiguous only if no more than three assignment options exist within the tolerance window, the chemical-shift deviation of this assignment is significantly smaller than for the other possibilities (at least 0.06 ppm), and the assignment is supported by other cross-peaks (>3) (16). All other cross-peaks were considered as ambiguous. Interprotomer distance restraints were unambiguously assigned only if they fulfilled the following criteria: (*i*) absence in the spectrum of the [UL-^{13}C$_6$]Glc 1:6 diluted sample, or presence only in the spectrum of the mixed [(1/2)-^{13}C] Glc-labeled sample compared with the spectra of the [1-^{13}C] Glc or [2-^{13}C] Glc

samples (48) and (*ii*) frequency unambiguous assignment within a ± 0.12-ppm tolerance window or network unambiguous; additional, optional criteria were (*iii*) at least two unambiguous cross-peaks for each pair of residues and (*iv*) cross-peak becomes frequency unambiguous in the PAIN spectra of [1-^{13}C] Glc or [2-^{13}C] Glc samples after all other intraprotomer assignment options were rejected in the protomer structure calculation.

Protomer Structure Calculation. The structure of the MAVS^{CARD} protomer (within the context of the filament) was calculated iteratively with ARIA 2.3 (28) and CNS software (33). Backbone dihedral angles were predicted with TALOS+ (25) from backbone chemical shifts, and predictions classified as "good" were converted into φ and ψ dihedral angle restraints. In addition, 86 hydrogen bonds, derived from TALOS+ secondary structure predictions, were introduced as distance restraints in the structure calculation. Both unambiguous and ambiguous distance restraints derived from ssNMR cross-peaks were applied with a flat-bottom harmonic potential using an upper bound of 8 Å. Structure calculation was performed using the following simulated annealing protocol: high-temperature sampling at 10,000 K (10,000 steps), the first annealing stage from 10,000 to 1,000 K (100,000 steps), and the second annealing stage from 1,000 to 50 K (60,000 steps). During the ARIA protocol, 60 conformers were calculated for the first eight iterations and 200 conformers were calculated in the final iteration. The 10 lowest energy structures were refined in a shell of water molecules. Table S3 provides a summary of ssNMR-derived restraints and statistics on the final ensemble of the protomer ssNMR structure.

Determination of the Helical Symmetry by Grid Search. Helical screw symmetry is defined by the azimuthal rotation (or rotational twist θ) around the helical axis and the axial translation (or rise r) along the helical axis between two consecutive subunits in a given start (Fig. 4*B*). Our grid-search approach systematically calculates conformations of 1-start helical filaments for given sets of helical parameters (θ, r) and uses the 10 best conformers of the ssNMR protomer ensemble as initial coordinates. For each (θ, r), 100 conformers were calculated (10 per randomly positioned initial protomer structure) by applying protomer-ambiguous interprotomer ssNMR restraints using CNS (33). The helical symmetry was imposed by strict noncrystallographic symmetry (NCS) constraints using 20 virtual copies of the central protomer (10 in each directions of the helical axis). The protocol to calculate a single helical conformation of 21 protomers consisted of (*i*) random positioning of the central protomer, (*ii*) a series of four rigid-body energy minimizations of 2,000 steps each, with decreasing values of force constant for the repulsive potential term (5.0–1.0), and (*iii*) 500 steps of flexible side chain minimization where backbone atoms were kept fixed. At each energy evaluation during minimizations, energetic contributions of interprotomer nonbonded interactions and distance restraints were computed by applying the helical symmetry operators (rotation of $k*\theta$ around and translation of $k*r$ along the arbitrarily chosen helical axis for k in $[-10,10]$) to the coordinates of the central protomer (32). During the rigid-body minimizations, the central protomer had all degrees of freedom. The PARALLHDG 5.3 force field was used in conjunction with a single repulsion energy term using PROLSQ parameters for nonbonded interactions (46). Interprotomer distance restraints were applied using a soft-square potential with a scale of 50 kcal/mol/A^2 and an upper limit of 8 Å. Because the symmetric copies of the central protomer were not modeled explicitly, interprotomer distance restraints were ambiguously applied between the central protomer (*m*) and its 20 symmetric copies (*p*) and averaged with "r^6 summation" (50) using the following equation:

$$d = \left(\sum_{p=1}^{20} \sum_{a}^{N_a} d_{a,m,p}^{-6} \right)^{-1/6},$$ [1]

where $d_{a,m,p}$ is the distance between a pair of atoms in protomers *m* and *p* corresponding to the *a*th assignment possibility of an interprotomer restraint. *n*-start helical conformations with cyclic C_n symmetry (*n* strands with *n*-fold rotational symmetry) were modeled by supplementing the set of helical strict NCS constraints with the appropriate rotational operators around the fixed helical axis ($n - 1$ rotations of 360°/*n*). The choice of the helical rotational axis has no influence on the outcome of the calculation because the modeled protomer is free to rotate and translate in all directions. The 2D grid-search was performed by repeating the protocol described above for all combinations of (θ,r) in the defined ranges and using increments of $\delta\theta$ for the twist angle and δr for the rise. Then, for each pair of (θ, r) explored in the grid, the median ($\tilde{E}$) of the total energy of the 20 lowest-energy helical conformers (among 100) was computed, and $\tilde{E}$ values

were smoothened by averaging the grid with a sliding square window of size ($3\delta\theta$, $3\delta r$). Such smoothing was intended to correct for unexplored (θ, r) due to the resolution of the grid (size of the increments $\delta\theta$, δr). Because the calculation of all individual helical conformations in the grid was independent from the others, the computational time can be greatly reduced by parallelizing the grid and dispatching the calculations on a computer cluster. To determine the helical parameters of MAVS^{CARD} filaments using ambiguous interprotomer distance restraints, a coarse-grained grid-search was first performed using increments of $\delta\theta = 2°$ for the twist and $\delta r = 0.2$ Å for the rise and modeling of 1-start left-handed, 1-start right-handed and 3-start C_3 helices. To further refine the symmetry parameters, a fine-grained grid-search was performed ($\delta\theta = 0.5°$ and $\delta r = 0.1$ Å) in a reduced range around the solution found with the coarse-grained search (left-handed, $100.0 \pm 5.0°$ and 5.5 ± 1.5 Å). This fine-grained search yielded a minimum for $\theta_{min} = 101°$ and $r_{min} = 5.1$ Å, values that were not explored in the coarse-grained search due to larger increments. Finally, a superfine-grained grid was computed using the final MAVS^{CARD} protomer structure as starting conformation and the protomer-unambiguous interprotomer distance restraints determined by ARIA. While using very small increments, the superfine-grained grid-search converged to the same symmetry parameters as the fine-grained search, thus confirming the accuracy of the grid-search approach. Details (θ and r ranges, increments, and computational times) for the coarse-, fine-, and superfine-grained grid-search are given in Table S4.

Validation of the Grid-Search Approach. A second coarse-grained search was performed using the 10 best conformers of the monomeric MAVS^{CARD} solution NMR ensemble as initial structures of the protomer. Using the same protocol, interprotomer restraints, and search criteria as previously described for the coarse-grained grid-search (helix type, twist/rise ranges, and increments), the absolute grid minimum was obtained for a left-handed helix with $\theta_{min} = 102°$ and $r_{min} = 5.6$ Å (the next minimum being $\theta = 102°$ and $r = 5.4$ Å; Fig. S4 *A and B*).

We further tested the grid-search methodology on a different helical assembly solved by ssNMR: the type III secretion system needle of *Salmonella typhimurium* (15). The initial atomic coordinates of the PrgI protomer structure and 162 interprotomer distance restraints were taken from PDB ID code 2LPZ (6). Helical symmetry was modeled using 30 copies of the central protomer (15 in both directions of the helical axis), and both left- and right-handed helices were tested. The grid ranges were set to [0°, 180°] for θ and [2.0 Å, 8.0 Å] for r using increments $\delta\theta = 2°$ and $\delta r = 0.2$ Å. The inner and outer diameters were restrained by imposing flat-bottom harmonic distance restraint between the Ca atoms of the PrgI protomer and the helical axis (lower bound of 12.5 Å and upper bound of 45 Å). The absolute grid minimum was obtained for a right-handed helix with $\theta_{min} = 64°$ and $r_{min} = 4.4$ Å (the second minimum being $\theta = 64°$ and $r = 4.2$ Å; Fig. S4 *C and D*).

Helical Filament Structure Calculation with ARIA. The helical structure of MAVS^{CARD} was automatically calculated with ARIA 2.3/CNS 1.2 (28, 33). The standard ARIA calculation protocols and CNS routines were modified to fix the helical symmetry during the simulated-annealing (SA) stage with the same constraint used in the grid search and described elsewhere (32, 51). The helical symmetry of the filament was modeled with a total of 11 protomers (five copies of the central protomer in both directions of the helical axis). The symmetry parameters imposing the helical symmetry were the ones obtained by the fine-grained grid-search ($\theta = 101°$ and $r = 5.1$ Å). Input distance restraints were (*i*) the refined set of intraprotomer restraints obtained by ARIA for the calculation of the protomer structure and (*ii*) protomer-ambiguous interprotomer restraints (not assigned to specific protomers). Assignment of protomer-ambiguous interprotomer distance restraints was performed using the atomic coordinates of the central protomer (M) and its six closest symmetric neighbors, corresponding to protomers M − 4, M − 3, M − 1, M + 1, M + 3, and M + 4. The threshold for considering a restraint as violated was set to 0.1 Å, whereas the ambiguity cutoff for filtering unlikely assignment possibilities was set to 0.8. In addition to the ssNMR distance restraints, the backbone dihedral angle and hydrogen-bond restraints used for the calculation of the protomer structure were also applied. To ensure convergence of the calculation, the total number of steps in the cooling stage of the simulated annealing was increased to 140,000, and 500 conformers were generated per iterations (of which the 15 lowest energy ones were analyzed). All other ARIA parameters were set to their default values. Convergence was reached after two iterations. ARIA automatically removed three interprotomer restraints and the number of unambiguous intraprotomer restraints increased. Statistics on the ssNMR filament structure are given in Table S3 and Fig. S3*B*.

Code Availability. An archive containing scripts and data for grid-search and ARIA calculations with helical symmetry may be downloaded at aria.pasteur. fr/supplementary-data/helical-ARIA.

Accession Codes. The solution state NMR structure of monomeric MAVS^{CARD} has been deposited under PDB ID code 2MS8. Chemical shift and restraint lists were deposited in BMRB under entry 25109. The ssNMR structure of the MAVS^{CARD} filament has been deposited under PDB ID code 2MS7. Chemical shift and restraint lists were deposited in BMRB under entry 25076.

1. Wu H (2013) Higher-order assemblies in a new paradigm of signal transduction. *Cell* 153(2):287–292.
2. Lu A, et al. (2014) Unified polymerization mechanism for the assembly of ASC-dependent inflammasomes. *Cell* 156(6):1193–1206.
3. Ge P, Zhou ZH (2011) Hydrogen-bonding networks and RNA bases revealed by cryo electron microscopy suggest a triggering mechanism for calcium switches. *Proc Natl Acad Sci USA* 108(23):9637–9642.
4. Yu X, Egelman EH (2010) Helical filaments of human Dmc1 protein on single-stranded DNA: A cautionary tale. *J Mol Biol* 401(3):544–551.
5. Xu H, et al. (2014) Structural basis for the prion-like MAVS filaments in antiviral innate immunity. *eLife* 3:e01489.
6. Wu B, et al. (2014) Molecular imprinting as a signal-activation mechanism of the viral RNA sensor RIG-I. *Mol Cell* 55(4):511–523.
7. Egelman EH (2014) Ambiguities in helical reconstruction. *eLife* 3:e04969.
8. Li J, Egelman EH, Craig L (2012) Structure of the Vibrio cholerae Type IVb Pilus and stability comparison with the Neisseria gonorrhoeae type IVa pilus. *J Mol Biol* 418(1-2):47–64.
9. Wasmer C, et al. (2008) Amyloid fibrils of the HET-s(218-289) prion form a beta so-lenoid with a triangular hydrophobic core. *Science* 319(5869):1523–1526.
10. Fitzpatrick AWP, et al. (2013) Atomic structure and hierarchical assembly of a cross-β amyloid fibril. *Proc Natl Acad Sci USA* 110(14):5468–5473.
11. Paravastu AK, Leapman RD, Yau W-M, Tycko R (2008) Molecular structural basis for poly-morphism in Alzheimer's beta-amyloid fibrils. *Proc Natl Acad Sci USA* 105(47):18349–18354.
12. Comellas G, Rienstra CM (2013) Protein structure determination by magic-angle spinning solid-state NMR, and insights into the formation, structure, and stability of amyloid fibrils. *Annu Rev Biophys* 42:515–536.
13. Schütz AK, et al. (2015) Atomic-resolution three-dimensional structure of amyloid β fibrils bearing the Osaka mutation. *Angew Chem Int Ed Engl* 54(1):331–335.
14. Lu J-X, et al. (2013) Molecular structure of β-amyloid fibrils in Alzheimer's disease brain tissue. *Cell* 154(6):1257–1268.
15. Loquet A, et al. (2012) Atomic model of the type III secretion system needle. *Nature* 486(7402):276–279.
16. Demers J-P, et al. (2014) High-resolution structure of the Shigella type-III secretion needle by solid-state NMR and cryo-electron microscopy. *Nat Commun* 5:4976.
17. Loquet A, et al. (2013) Atomic structure and handedness of the building block of a biological assembly. *J Am Chem Soc* 135(51):19135–19138.
18. Egelman EH (2010) Reconstruction of helical filaments and tubes. *Methods Enzymol* 482:167–183.
19. Yoneyama M, Onomoto K, Jogi M, Akaboshi T, Fujita T (2015) Viral RNA detection by RIG-I-like receptors. *Curr Opin Immunol* 32:48–53.
20. Hou F, et al. (2011) MAVS forms functional prion-like aggregates to activate and propagate antiviral innate immune response. *Cell* 146(3):448–461.
21. Ferrao R, Wu H (2012) Helical assembly in the death domain (DD) superfamily. *Curr Opin Struct Biol* 22(2):241–247.
22. Potter JA, Randall RE, Taylor GL (2008) Crystal structure of human IPS-1/MAVS/VISA/Cardif caspase activation recruitment domain. *BMC Struct Biol* 8:11.
23. He L, Lührs T, Ritter C (2015) Solid-state NMR resonance assignments of the filament-forming CARD domain of the innate immunity signaling protein MAVS. *Biomol NMR Assign* 9(2):223–227.
24. Loquet A, Giller K, Becker S, Lange A (2010) Supramolecular interactions probed by 13C-13C solid-state NMR spectroscopy. *J Am Chem Soc* 132(43):15164–15166.
25. Shen Y, Delaglio F, Cornilescu G, Bax A (2009) TALOS+: A hybrid method for pre-dicting protein backbone torsion angles from NMR chemical shifts. *J Biomol NMR* 44(4):213–223.
26. Hong M (1999) Determination of multiple ***φ***-torsion angles in proteins by selective and extensive (13)C labeling and two-dimensional solid-state NMR. *J Magn Reson* 139(2):389–401.
27. Castellani F, et al. (2002) Structure of a protein determined by solid-state magic-angle-spinning NMR spectroscopy. *Nature* 420(6911):98–102.
28. Bardiaux B, Malliavin T, Nilges M (2012) ARIA for solution and solid-state NMR. *Methods Mol Biol* 831:453–483.
29. Pierce B, Tong W, Weng Z (2005) M-ZDOCK: A grid-based approach for Cn symmetric multimer docking. *Bioinformatics* 21(8):1472–1478.
30. Potluri S, Yan AK, Chou JJ, Donald BR, Bailey-Kellogg C (2006) Structure determination of symmetric homo-oligomers by a complete search of symmetry configuration space, using NMR restraints and van der Waals packing. *Proteins* 65(1):203–219.
31. Wang X, Bansal S, Jiang M, Prestegard JH (2008) RDC-assisted modeling of symmetric protein homo-oligomers. *Protein Sci* 17(5):899–907.
32. Bardiaux B, van Rossum B-J, Nilges M, Oschkinat H (2012) Efficient modeling of symmetric protein aggregates from NMR data. *Angew Chem Int Ed Engl* 51(28):6916–6919.
33. Brunger AT (2007) Version 1.2 of the Crystallography and NMR system. *Nat Protoc* 2(11):2728–2733.
34. Rieping W, et al. (2007) ARIA2: Automated NOE assignment and data integration in NMR structure calculation. *Bioinformatics* 23(3):381–382.
35. Egelman EH, Francis N, DeRosier DJ (1982) F-actin is a helix with a random variable twist. *Nature* 298(5870):131–135.
36. Peisley A, Wu B, Xu H, Chen ZJ, Hur S (2014) Structural basis for ubiquitin-mediated antiviral signal activation by RIG-I. *Nature* 509(7498):110–114.
37. Peisley A, Wu B, Yao H, Walz T, Hur S (2013) RIG-I forms signaling-competent fila-ments in an ATP-dependent, ubiquitin-independent manner. *Mol Cell* 51(5):573–583.
38. Lu A, et al. (2015) Plasticity in PYD assembly revealed by cryo-EM structure of the PYD filament of AIM2. *Cell Discov* 1:15013.
39. Sgourakis NG, et al. (2011) Determination of the structures of symmetric protein oligomers from NMR chemical shifts and residual dipolar couplings. *J Am Chem Soc* 133(16):6288–6298.
40. Mashiach-Farkash E, Nussinov R, Wolfson HJ (2011) SymmRef: A flexible refinement method for symmetric multimers. *Proteins* 79(9):2607–2623.
41. Karaca E, Melquiond ASJ, de Vries SJ, Kastritis PL, Bonvin AMJJ (2010) Building macromolecular assemblies by information-driven docking: Introducing the HADDOCK multibody docking server. *Mol Cell Proteomics* 9(8):1784–1794.
42. Tang M, Comellas G, Rienstra CM (2013) Advanced solid-state NMR approaches for structure determination of membrane proteins and amyloid fibrils. *Acc Chem Res* 46(9):2080–2088.
43. Tycko R (2011) Solid-state NMR studies of amyloid fibril structure. *Annu Rev Phys Chem* 62:279–299.
44. Morag O, Sgourakis NG, Baker D, Goldbourt A (2015) The NMR-Rosetta capsid model of M13 bacteriophage reveals a quadrupled hydrophobic packing epitope. *Proc Natl Acad Sci USA* 112(4):971–976.
45. Das R, et al. (2009) Simultaneous prediction of protein folding and docking at high resolution. *Proc Natl Acad Sci USA* 106(45):18978–18983.
46. Linge JP, Nilges M (1999) Influence of non-bonded parameters on the quality of NMR structures: A new force field for NMR structure calculation. *J Biomol NMR* 13(1):51–59.
47. Gardiennet C, et al. (2012) A sedimented sample of a 59 kDa dodecameric helicase yields high-resolution solid-state NMR spectra. *Angew Chem Int Ed Engl* 51(31):7855–7858.
48. Loquet A, Lv G, Giller K, Becker S, Lange A (2011) 13C spin dilution for simplified and complete solid-state NMR resonance assignment of insoluble biological assemblies. *J Am Chem Soc* 133(13):4722–4725.
49. Vranken WF, et al. (2005) The CCPN data model for NMR spectroscopy: Development of a software pipeline. *Proteins* 59(4):687–696.
50. Nilges M (1993) A calculation strategy for the structure determination of symmetric dimers by 1H NMR. *Proteins* 17(3):297–309.
51. Campos M, Francetic O, Nilges M (2011) Modeling pilus structures from sparse data. *J Struct Biol* 173(3):436–444.
52. Valentine RC, Shapiro BM, Stadtman ER (1968) Regulation of glutamine synthetase. XII. Electron microscopy of the enzyme from Escherichia coli. *Biochemistry* 7(6):2143–2152.
53. Güntert P, Dötsch V, Wider G, Wüthrich K (1992) Processing of multi-dimensional NMR data with the new software PROSA. *J. Biomol NMR* 2(6):619–629.
54. Keller RLJ (2005) Optimizing the process of nuclear magnetic resonance spectrum analysis and computer aided resonance assignment. PhD dissertation (Swiss Federal Institute of Technology, Zurich). ETH No. 15947.
55. Kay LE, Torchia DA, Bax A (1989) Backbone dynamics of proteins as studied by 15N inverse detected heteronuclear NMR spectroscopy: Application to staphylococcal nuclease. *Biochemistry* 28(23):8972–8979.
56. Guerry P, Herrmann T (2012) Comprehensive automation for NMR structure de-termination of proteins. *Methods Mol Biol* 831:429–451.
57. Doreleijers JF, et al. (2012) CING: An integrated residue-based structure validation program suite. *J Biomol NMR* 54(3):267–283.
58. Bakan A, Meireles LM, Bahar I (2011) ProDy: Protein dynamics inferred from theory and experiments. *Bioinformatics* 27(11):1575–1577.
59. Pintar A, Carugo O, Pongor S (2003) DPX: for the analysis of the protein core. *Bioinformatics* 19(2):313–314.
60. Hubbard SJ, Thornton JM (1993) *NACCESS, Computer Program* (Department of Bio-chemistry and Molecular Biology, University College London).
61. Dosset P, Hus JC, Blackledge M, Marion D (2000) Efficient analysis of macromolecular rotational diffusion from heteronuclear relaxation data. *J Biomol NMR* 16(1):23–28.

He et al.